Research Square

Preprints are preliminary reports that have not undergone peer review.
They should not be considered conclusive, used to inform clinical practice,
or referenced by the media as validated information.

# Atomic-scale mechanism for shock-induced ambient-stable hexagonal close-packed Iron

**Mao Liu**

liumao@mail.neu.edu.cn

Northeastern University https://orcid.org/0000-0003-1853-5583

**Jiamu Liu**

Northeastern University

**Jianxing Liu**

Northeastern University

**Pengfei Wang**

University of Science and Technology of China https://orcid.org/0000-0002-9924-8537

**Jian Wang**

University of Nebraska-Lincoln https://orcid.org/0000-0001-5130-300X

**Hao Ding**

Harbin Institute of Technology

**Tingting Huang**

University of Science and Technology of China

**Mingyu Gong**

Shanghai Jiao Tong University https://orcid.org/0000-0002-8120-5264

**Article**

**Keywords:**

**Posted Date:** March 5th, 2026

**DOI:** https://doi.org/10.21203/rs.3.rs-8878778/v1

**License:** This work is licensed under a Creative Commons Attribution 4.0 International License.
Read Full License

**Additional Declarations:** There is **NO** Competing Interest.

# Title: Atomic-scale mechanism for shock-induced ambient-stable hexagonal close-packed Iron

**Authors:** Jiamu Liu[1]†, Jianxing Liu[1]†, Pengfei Wang[2]†, Jian Wang[3]*, Hao Ding[4], Tingting Huang[2], Mingyu Gong[5], Mao Liu[1]*

## Affiliations

[1]School of Metallurgy, Northeastern University, Shenyang 110819, China.
[2]CAS Key Laboratory of Mechanical Behavior and Design of Materials, University of Science and Technology of China, Hefei 230027, China.
[3]Department of Mechanical and Materials Engineering, University of Nebraska, Lincoln 68588, USA.
[4]Hunan Aviation Powerplant Research Institute, Aero Engine (Group) Corporation of China, Zhuzhou 412002, China.
[5]State Key Lab of Metal Matrix Composites, School of Materials Science and Engineering, Shanghai Jiao Tong University, Shanghai 200240, China.

†These authors contributed equally to this work.

*Corresponding authors: Email: jianwang@unl.edu（Jian Wang);

liumao@mail.neu.edu.cn (Mao Liu)

## Abstract

**Hexagonal close-packed (hcp) ε-Fe has traditionally been thought to exist only under high-pressure conditions, such as the Earth's core. According to conventional understanding, once the pressure is released, hcp ε-Fe immediately reverts to body-centered cubic (bcc) α-Fe, and its stable presence has never been directly observed. In this study, we report the first direct atomic-scale observation of hcp ε-Fe in high-purity single-crystal Fe subjected to ultrahigh-strain-rate dynamic shock loading. Remarkably, the hcp ε-Fe phase persists stably even after pressure release, challenging the long-standing transition theory that has prevailed for the past 70 years. We propose a novel phase transition mechanism to account for this observation. These findings open new pathways for exploring the properties and potential applications of hcp ε-Fe.**

## Main Text

Fe is one of the most abundant elements on Earth, predominantly found in the forms of body-centered cubic (bcc) α-Fe and face-centered cubic (fcc) γ-Fe. Besides this, hexagonal close-packed (hcp) ε-Fe is a primary component of the Earth's inner core due to high hydrostatic pressure[1–4]. ε-Fe exhibits superior strength and non-magnetism compared to bcc α-Fe[5,6]. These properties provide ε-Fe with significant advantages in various fields, including superconductivity[7,8], electronic and magnetic[9], etc. A detailed understanding of the Fe phase diagram has been systematically investigated for more than half a century[2,10–18]. Although α-Fe begins its transition to the hcp structure at an applied pressure of 13 GPa at room temperature[16,19,20], ε-Fe remains stable only if the pressure is maintained at a minimum of 300 GPa[21]. A prevailing view is that ε-Fe can only exist under high-pressure conditions[22–24]. The relationship of Fe have been systematically investigated for more than half a century, resulting in a detailed understanding of the Fe phase diagram[2,18].

The martensitic bcc-to-hcp phase transition in Fe has attracted considerable attention across multiple research fields[2,16,25–27]. This interest stems not only from the geophysical and societal importance of Fe but also from the significant technological challenge posed by the inherent instability of the hcp phase, which, according to classical reverse transition theory, tends to revert to its original bcc structure[28]. Atomic-level simulations have played a crucial role in complementing experimental studies, particularly in exploring the kinetics and dynamics of the bcc-to-hcp phase transition. Nucleation and growth of hcp domains within the bcc matrix have been extensively studied using molecular dynamics (MD) simulations under shock loading conditions, offering insights into the role of defects, dislocations, and grain boundaries in promoting or inhibiting the phase transition[20]. Despite these advancements, the accuracy of simulations remains limited by the quality of empirical interatomic potentials and the

computational cost of simulating large systems over long timescales. Moreover, the discrepancy between timescales in simulations and experiments presents another major challenge. MD simulations typically operate on nanosecond timescales, while real-world experiments involve significantly longer timescales, making direct comparisons difficult. It is worth noting that most MD simulations have focused on the phase transition of shock loaded single-crystal Fe[13,20,29]. Another concern is that previous MD studies were based on the hypothetical reverse transition theory, which assumes that the α-ε phase transition in Fe preferentially propagates along $\{11\bar{2}\}$ planes under the high pressure and reverses along the same path once the pressure is released[28]. However, stable hcp ε-Fe has never been directly observed at either micro- or atomic-scale in shock-loaded Fe samples during real experimental tests, providing no solid evidence confirming that the α-ε phase transition in Fe preferentially propagates along $\{11\bar{2}\}$ planes. Furthermore, the (001) crystallographic plane is typically used to study the bcc-to-hcp phase transition[29–31]. A natural question arises: can the hcp structure stably exist within a bcc Fe matrix subjected to shock along other planes, such as (110)?

The main debate continues over whether hcp ε-Fe remains stable under ambient conditions or inevitably reverts to the bcc structure once the pressure is released. According to the reverse transition theory[28], hcp structure forms only transiently under high-pressure shock loading, typically around 13 GPa[16,20], and immediately reverts to the original bcc structure once the shock pressure is released. Consequently, this reversible bcc-to-hcp phase transition leaves no trace of the hcp-phase, making it impossible to directly observe in the microstructure of postmortem samples[20,28]. Earlier experimental methods relied primarily on indirect wave profile measurements[16,28,32–35], which could not provide conclusive evidence of the bcc-to-hcp phase transition. Recent advances in extended x-ray absorption fine structure (EXAFS) techniques have detected diffraction patterns corresponding to the hcp phase in both single-crystal and

polycrystalline Fe[30,31,36,37]. Nevertheless, even with these advancements, EXAFS remains incapable of directly capturing the morphological features or imaging the microstructures that characterize the bcc-to-hcp phase transition.

In this study, we demonstrated that stable hcp phases can be directly imaged at the atomic scale in recovered high-purity (99.99 wt% purity) bcc Fe single-crystals, which was shocked by the Split Hopkinson Pressure Bar (SHPB) at both 77k and room temperature. (110) plane was finally ensured to be the shocked plane in this study. Atomic scale hcp structures were directly imaged by the spherical aberration corrected Scanning Transmission Electron Microscopy (ac-STEM). Our results demonstrate a practical route to achieve stable hcp ε-Fe. This discovery challenges the conventional understanding of hcp ε-Fe and its existence under extreme conditions, providing new insights into its potential applications. The ability to stabilize hcp ε-Fe at normal pressure presents opportunities to study its unique characteristics in more depth, such as its strength, ductility, and resistance to deformation, which could have significant implications for materials science and industrial applications.

## Results and Discussion

The SHPB system (Fig. 1a) [38] was employed to apply extremely high stress to the high-purity (99.99 wt% purity) single-crystal Fe at 77K with an initial shock speed of 38 m/s. The engineering stress reached up to 17.6 GPa, with a maximum strain rate of $1.96 \times 10^4/s$. The sample is instantly compressed to approximately one-tenth (~200 μm) of its original thickness (2 mm), a process known as dynamic plastic deformation[39]. The initial orientation of the disk surface was (110), namely the initial normal direction (ND) || (110) (Fig. 1b). The Focused Ion Beam (FIB) technique was employed to precisely etch the sample into nanoscale slices for further analysis (Supplementary Fig. 1). The microstructure of the sample was examined using Transmission Electron Microscopy (TEM) as shown in Fig. 1d. The TEM images reveal a high concentration of clustered dislocation lines and a fine grain structure across the sample. Upon magnification, as illustrated in Fig. 1e, the dislocation dense regions exhibit a wavy, river-like pattern, consistent with the transmission morphology typically observed in samples subjected to severe plastic deformation[40,41].

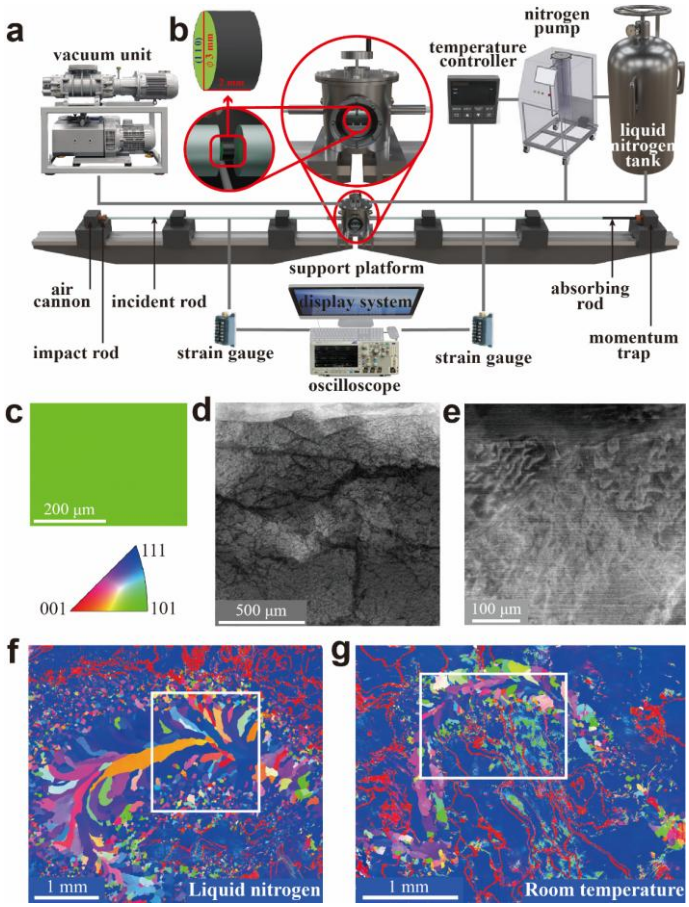



**Fig. 1 Schematic diagram of SHPB and microstructure characterizations of deformed single-crystal Fe.** (**a**) Integrated SHPB experimental platform for high-strain-rate impact testing, comprising an impact assembly, vacuum and temperature control systems, a cryogenic vacuum chamber, and a high-speed data acquisition system. (**b**) Schematic illustration of a single-crystal Fe sample positioned within the cryogenic vacuum chamber. The cylindrical specimen, measuring ⌀3 × 2 mm, features a smoothly polished surface with the (110) crystallographic plane highlighted in green. (**c**) EBSD inverse pole figure (IPF) map of the pristine single-crystal Fe, confirming the (110) surface orientation. (**d and e**) TEM image showing the microstructural evolution of single-crystal Fe at 77 K. High-density dislocations and river-like patterns are evident, reflecting significant plastic strain. (**f and g**) Large-area montaged EBSD map showing the microstructural evolution of single-crystal Fe subjected to ultrahigh-strain-rate impact at 77 K and temperature. The initial (110) matrix has undergone a complete crystallographic reorientation to (111). The deformation pattern features a petal-like central zone, from which elongated (001)-oriented lamellar grain strips radiate toward the periphery. Detailed features within the white box region are provided in Supplementary Fig. S2.

The original sample surface prepared for shock loading was examined by Electron Back Scatter Diffraction (EBSD), as shown in Fig. 1c, confirming its (110) orientation. A large-area EBSD image of samples shocked at liquid nitrogen temperature (77 K) is shown in Fig. 1f. The

results reveal that shock loading induced a pronounced crystallographic reorientation within the single-crystal Fe, with the orientation shifting from (110) to predominantly (111). This change is visually represented by a color shift from pure green in Fig. 1c to predominantly blue in Fig. 1f. To further confirm the reorientation behavior, a lower shock speed (16 m/s) was applied to a sample of the same size at room temperature. The corresponding large-area EBSD image (Fig. 1g) similarly shows the orientation shifting from (110) to predominantly (111).

On the reoriented (111) plane, phase transition of hcp ε-Fe was observed. This process of crystal reorientation may be key to initiating the phase transition and stabilizing the existence of hcp ε-Fe. This mechanism differs from the previously reported transition theory based on the Burgers orientation relationship[20,28], which proposes that the α-ε phase transition in Fe preferentially propagates along $\{11\bar{2}\}$ planes under high pressure and reverses along the same path once the pressure is released.

Large-area EBSD imaging of cryogenically shock-loaded Fe (Fig. 1f) reveals small, fragmented grains (Supplementary Fig. 2) surrounded by grains exhibiting a (001) orientation extending outward from the core. The room-temperature group (Fig. 1g) displayed similar features to the liquid-nitrogen group (Fig. 1f), although cryogenic shock loading produced finer grains (comparison of Fig. 1f, 77 K, and Fig. 1g, room temperature). This refinement is likely due to the combined effects of deformation strain induced by shock speed and the reduced nucleation barrier at lower temperatures[42–44], which facilitates easier polycrystallization in the single-crystal sample[38].

Such a large-scale tilt in matrix crystal orientation—from (110) to predominantly (111)—induced by ultrahigh-strain-rate shock loading has not been previously reported. Further investigation of the phase transition mechanism indicates that this extensive orientation tilting is critical for initiating and stabilizing the hcp phase. Consequently, the transition pathway observed here is fundamentally distinct from the classical Burgers orientation relationship theory[20,28]. In our

study, the α-ε phase transition does not propagate along $\{11\bar{2}\}$ planes, which explains why the hcp phase does not revert to the bcc phase via conventional reverse transition mechanisms[20,28].

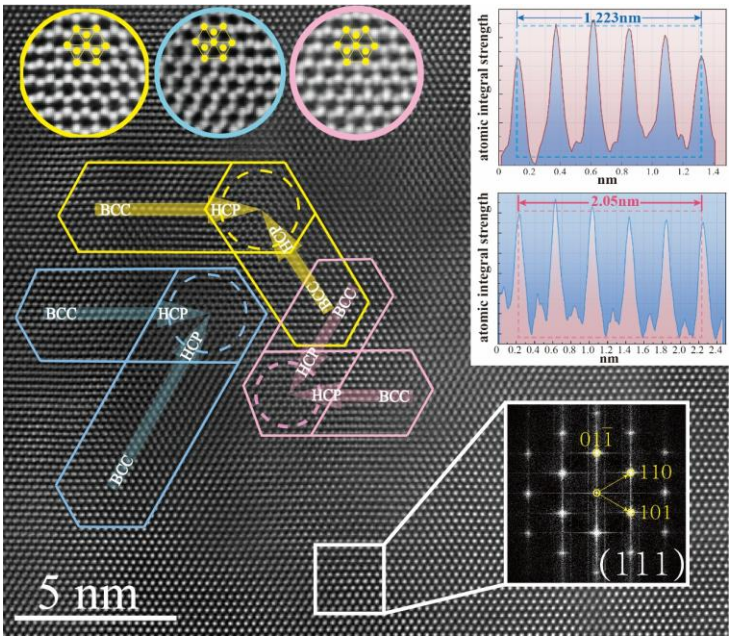



**Fig. 2 HAADF-STEM image showing the hcp Fe formed after ultrahigh-strain-rate shock loading at 77K.** Three color-coded polygons delineate the crystallographic pathways of the bcc-to-hcp phase transition, illustrating a characteristic core-shell distribution with an hcp core encapsulated by a bcc periphery. The region encapsulated by the dashed circle is shown as a magnified view in the top inset, revealing distinct ring-like features corresponding to the hcp (0001) plane. The selected area electron diffraction (SAED) pattern in the bottom-right white box confirms the (111) orientation of the matrix. Furthermore, the extracted lattice parameters provided in the top-right corner validate the structural identification of both bcc and hcp phases, substantiating an orientation relationship of bcc (111) || hcp (0001).

The hcp ε-Fe phase was directly identified in high-purity single-crystal Fe following ultrahigh-strain-rate shock along the bcc [110] axis using ac-STEM. This finding represents a significant departure from the prevailing understanding over the past 70 years[16,32,45,46], which consistently suggested that hcp ε-Fe exists only under high-pressure conditions. In contrast, our results demonstrate that hcp ε-Fe can remain stable under ambient pressure—an observation not previously reported in the literature.

Figure 2 shows an ac-STEM image of the matrix with a (111) orientation, along with the corresponding Selected Area Electron Diffraction (SAED) pattern highlighted in the purple box

below. The hcp ε-Fe phase, oriented parallel to (0001), is observed in multiple regions. On the left side of Fig. 2, three distinct hcp ring-like features are highlighted by yellow, blue, and pink circles. These observations reveal a clear crystallographic orientation relationship between bcc and hcp structures, specifically bcc (111) || hcp (0001), with a structural diagram provided in Supplementary Fig. 3b. The interatomic distances for both bcc and hcp phases were measured and verified. As shown in the box in the top-right corner of Fig. 2, the theoretical distance between adjacent atoms in bcc Fe is 4.05 Å, with a measured value of 4.10 Å. For the hcp Fe structure, the predicted distance is 2.45 Å, with a measured value of 2.446 Å. These measurements confirm the bcc-to-hcp phase transition, with the hcp features appearing to emerge from the surrounding bcc structures, indicating a structural transformation. Supplementary Fig. 4 presents an ac-STEM image of another region from the same deformed single-crystal Fe at 77 K. The hcp features are highlighted by colored rectangles, with magnified views shown in Supplementary Fig. 4c-g. The observed hcp structures can be interpreted as stable morphological configurations, likely encompassing multiple intermediate stages that reflect the complex phase transition pathway.

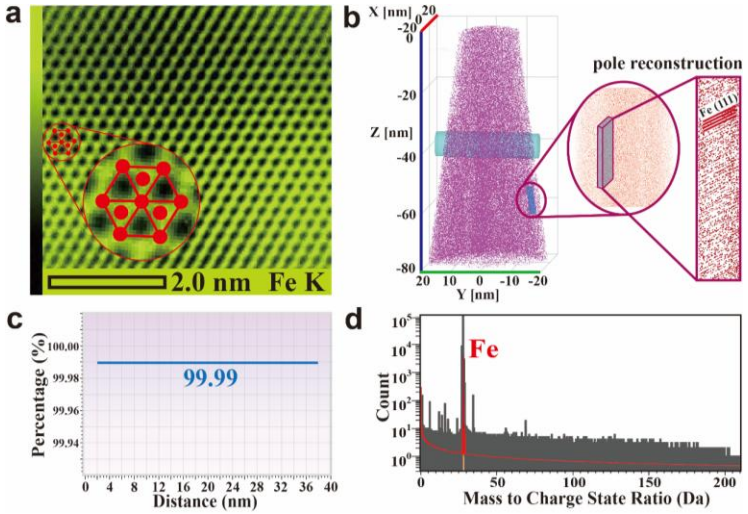



**Fig. 3 Atomic-eds and APT analysis of high-purity Fe.** (**a**) Atomic-resolution EDS mapping of the hcp-Fe phase via aberration-corrected STEM with a continuous 5-minute dwell time. The well-preserved atomic features demonstrate the exceptional structural stability and radiation hardness of the hcp-Fe phase against electron-beam irradiation. (**b**) APT reconstruction obtained via field evaporation of a needle-shaped sample, extracted from a deformed single-crystal Fe region

containing the hcp phase. Following OIM-based post-processing and pole reconstruction, the orientation-specific atomic arrangement in the high-purity metal is resolved, revealing a well-defined stacking of {111} crystallographic planes. (**c**) One-dimensional (1D) concentration profile extracted from the blue cylindrical region of interest (ROI) indicated in (**b**). The elemental analysis confirms a high chemical purity of 99.99% Fe for the single-crystal sample. (**d**) Mass-to-charge ratio spectrum of deformed Fe acquired during APT analysis, further substantiating the exceptional chemical purity of the specimen. The absence of any extraneous mass peaks beyond Fe corroborates the high purity level.

To verify that the α-Fe to ε-Fe phase transition was solely induced by ultrahigh-strain-rate shock loading of high-purity single-crystal (110) Fe—rather than by impurities or chemical alterations—samples were carefully prepared for analysis using Energy Dispersive Spectroscopy (EDS) and Three-Dimensional Atom Probe Tomography (3D-APT). This preparation ensured accurate assessment of the transition mechanism while ruling out external influences. Focused Ion Beam (FIB) processing (Supplementary Fig. 1) was used to prepare the samples. Fig. 3a shows the EDS image of the hcp ε-Fe phase. Throughout a 15-minute EDS scan, the hcp structure remained stable, and no additional elements forming regular atomic structures were detected, confirming that the observed hcp phase consists purely of Fe. This demonstrates that the phase transition is intrinsic to high-purity Fe and not influenced by impurities.

Figure 3b presents the 3D-APT results, revealing a uniform atomic distribution. The (111) orientation is clearly identifiable through pole reconstruction using Orientation Imaging Microscopy (OIM) analysis. Within the selected cuboid region in Fig. 3b, Fe atoms follow the (111) α-Fe orientation, with a measured interatomic distance of 1.67 Å, consistent with the expected spacing for (111) α-Fe. To further examine the composition, a Region of Interest (ROI) in the form of a blue cylinder was selected on the APT needle for line scanning, with the resulting data shown in Fig. 3c.

Figure 3d displays the mass spectrum, representing the atomic mass distribution of all detected atoms during the APT process. If atoms of other elements were present, distinct peaks

would appear at their corresponding mass-to-charge ratios. However, no peaks corresponding to elements other than Fe are observed, confirming the sample's extremely high purity. Therefore, the observed atomic structure can be unequivocally attributed to hcp ε-Fe, providing strong evidence that the phase transition results entirely from the mechanical impact of ultrahigh-strain-rate shock loading on high-purity Fe, without contamination or chemical interference.

The phase transition mechanism from the bcc to hcp structure under ultrahigh-strain-rate shock was further elucidated by a theoretical model. As illustrated in Fig. 4a, applying an ultrahigh-strain-rate shock along the [110] direction to the bcc matrix induced significant crystal reorientation and lattice distortion across the crystal structure. The shock loading caused a broad reorientation of the single-crystal Fe from its original (110) orientation to predominantly (111), as confirmed by previous HAADF-STEM (Fig. 2 and Supplementary Fig. 4) and EBSD images (Fig. 1c, f and g). The dominance of (111) orientations in the large scale EBSD image after deformation might be the result of a combination of lattice rotation, slip system activity, and deformation induced dynamic recrystallization[38]. These mechanisms work together to reorient the bcc Fe crystal lattice in response to the extreme conditions of shock loading. This crystallographic orientation change results in a stable orientation relationship, aligning bcc (111) with hcp (0001). Additionally, the shock loading introduced notable lattice distortion, including elongation (compression), twisting (shear), and atomic shift (shuffle). During compression, the unit cell stretches along the [111] direction (Fig. 4b), while the shear process (Fig. 4c) causes the unit cell to twist around the [111] axis[28,47,48]. Following compression and shear, the shuffle process (Fig. 4d) completes the phase transition by causing the vertex atoms in the original bcc structure to shift parallel to the (0001) plane of the hcp structure. The distinct roles of compression, shear, and shuffle in this transition are illustrated in Fig. 4b-d, with each mechanism contributing to the structural evolution during shock loading.

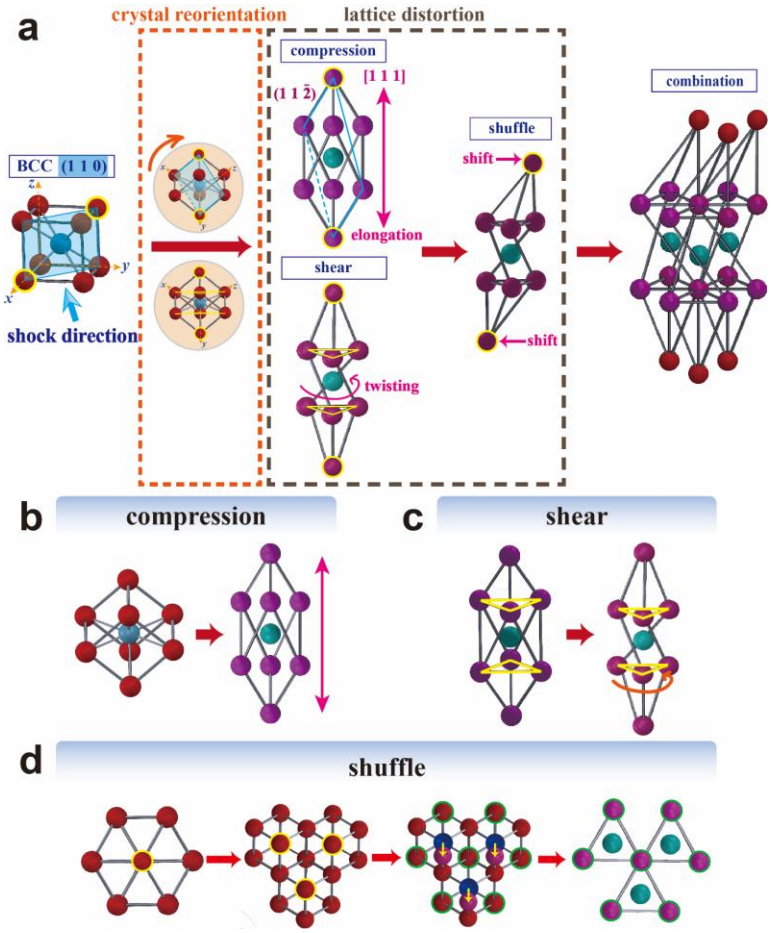



**Fig. 4 Transition mechanism of bcc→hcp for high-purity single-crystal Fe.** (**a**) Schematic illustration of the bcc→hcp phase transition mechanism, substantiating a purely mechanical deformation pathway. Blue arrows denote the ultrahigh-strain-rate impact along the [110] direction. The transition initiates with a crystal reorientation from (110) to (111), consistent with the EBSD observations. This is followed by lattice distortion involving three sequential processes: compression, shear, and shuffle, which correspond to lattice elongation, twisting, and shift, respectively. (**b**) Compression process along [111] direction. (**c**) Shear process drives layers of atoms twisting. (**d**) Shuffle process shifts atoms into the lowest energy position.

After the compression, shear, and shuffle processes, the resulting unit cells stack and form a cohesive three-dimensional structure, as depicted in Supplementary Fig. 3a. The bcc structure appears on the left, transiting into the hcp structure on the right, with the purple line marking the boundary of the hcp unit cell. HAADF-STEM imaging (Fig. 2 and Supplementary Fig. 4) confirms the orientation relationship between the two structures, with bcc (111) aligned parallel to hcp (0001). This orientation alignments provide critical insights into the atomic-scale mechanisms

underlying the bcc-to-hcp phase transition. Additional orientation relationships pertinent to the observable crystal plane are illustrated in Supplementary Fig. 3b, depicting vertical orientation relationships— bcc $(11\bar{2})$ aligning with hcp $(11\bar{2}0)$, and bcc (110) aligning with hcp $(10\bar{1}0)$. STEM images acquired along these orientations fail to resolve complete atomic arrangements and phase transition dynamics due to interatomic distances falling below the resolution of aberration-corrected microscope. Nevertheless, through HAADF-STEM along [111], the aforementioned orientation relationships have been conclusively confirmed. This comprehensive visualization sheds light on the atomic rearrangement during the phase transition and clarifies the crystallographic changes that occur throughout the process.

Notably, the atomic rearrangement pathway between the bcc and hcp structures in Fe involves complex transitional states, as these phases are not directly adjacent. Our theory indicates that under ultrahigh-strain-rate shock loading, bcc Fe undergoes a structural transformation that terminates at the hcp phase. This process exhibits a continuous structural gradient: regions experiencing deeper transformation adopt a lattice configuration closer to hcp, while shallower regions retain bcc ordering. As a result, the thermodynamically stable configuration within the bcc matrix is a spatially heterogeneous structure centered around an hcp core. This metastable architecture (Fig. 5b) comprises an hcp nucleus (<30 nm) enveloped by a coherent transition layer that gradually approaches bcc structure. The atomically smooth gradient across this transition layer minimizes lattice misfit strain, providing optimal atomic accommodation. Atomic-scale stress concentration mapping (Fig. 5c and d) visually demonstrates the strain energy confining the hcp core. The spatial configuration of this transition layer is governed by the dual coherency requirement with the adjacent phases. Its inner facet maintains a specific orientation relationship with the hcp phase, while the outer facet maintains with the bcc matrix. The octahedral model in Fig. 5b, derived from the crystallographic correspondence in Fig. 5a, represents the lowest nuclear

energy solution with the lowest index facets which can achieve a closed topology. Crucially, the nucleation barrier for this hcp-core structure is substantially lower than that for direct hcp nucleation within bcc. This energetically favored pathway fundamentally explains the unprecedented existence of hcp phase without reverse transition to bcc. Fig. 5e-h illustrate the bcc →hcp transition pathways along two different directions, which correlate with the localized lattice distortions observed in the aforementioned strain concentration zones.

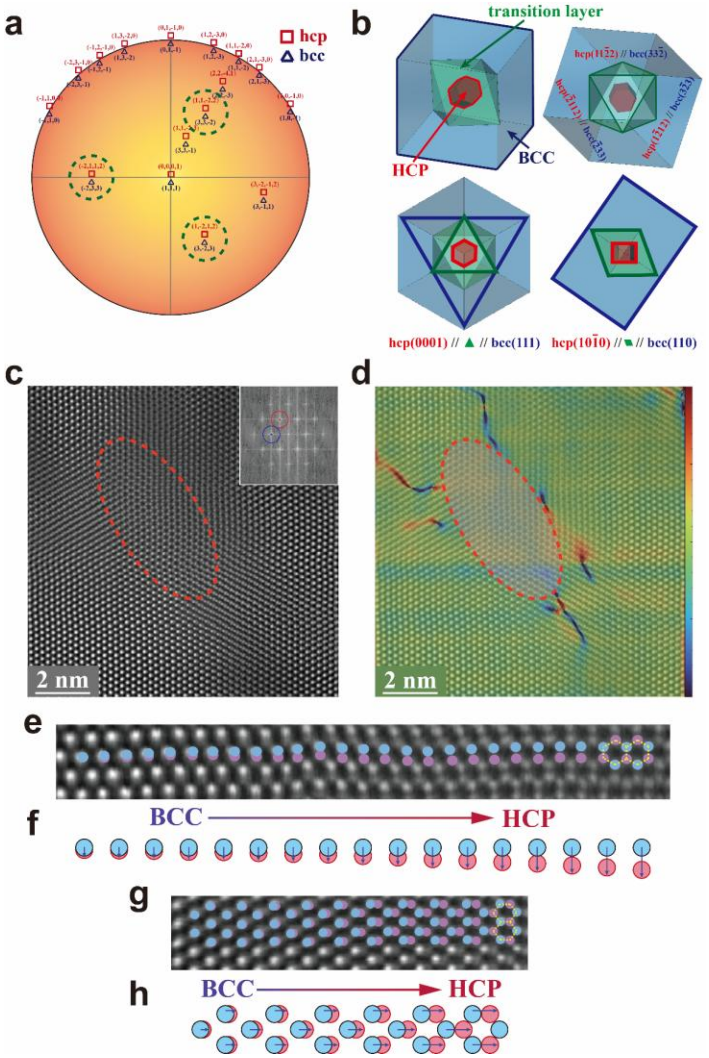



**Fig. 5 Crystallographic correspondences and atomic-scale stress concentration.** (**a**) Composite pole figures illustrating the orientation relationship between the bcc and hcp phases. hcp and bcc structures are denoted by red squares and blue triangles (with corresponding miller indices), respectively. The plots selectively display positions where the orientation relationship is satisfied, revealing a unique correspondence between each red square and blue triangle. The dashed circles highlight three centrosymmetric orientations, and these three sets of low-index

planes form a spatial enclosure, representing the lowest-energy configuration for encapsulating the hcp core. (**b**) Based on the three orientations marked by green dashed circles in (**a**) and the established bcc (111) || hcp (0001) relationship, a spatial structural model is constructed. These four orientation relationships collectively define an octahedral geometry that forms the outermost boundary of the hcp core. The interior of this structure consists of a central hcp nucleus surrounded by a complex transitional zone, while the exterior is directly adjacent to the bcc matrix. The two schematics below provide alternative perspectives from different viewing directions. (**c**) HAADF-STEM image of the hcp structure with an inset showing the geometric phase analysis (GPA) -derived diffraction representation of atomic spacing in the indicated region. (**d**) GPA-derived strain map of the hcp nucleus, outlined by the red dashed oval, corresponding to (**c**). This illustrates a significant nanoscale strain concentration in the adjacent areas. (**e**) Atomic arrangement within the hcp nucleus as viewed from a specific projection in (**d**). The displacement of individual atomic rows is observed to be orthogonal to the phase transition direction, ultimately constituting a characteristic crystallographic plane of the hcp structure. (**f**) Schematic representation of the theoretical model illustrated in (**e**). (**g**) Analogous to (**e**), the displacement of atomic rows occurs parallel to the phase transition direction, leading to the formation of a specific crystallographic plane in the hcp structure. (**h**) Schematic representation of the theoretical model illustrated in (**g**).

Our results provide compelling evidence that challenges the long-standing assumption that hcp Fe exists only under high pressure and that the bcc–hcp transition strictly follows the Burgers orientation relationship. By applying ultrahigh-strain-rate shock loading to single-crystal Fe, we observed extensive crystal reorientations, which serve as a critical trigger for the phase transition. Direct atomic-resolution HAADF-STEM imaging of hcp Fe, corroborated by EDS and APT analyses, confirms that the phase transition is driven solely by structural rearrangement. We propose a comprehensive theoretical model of the phase transition, integrating the atomic deformation mechanisms within single-crystal Fe, the overall atomic arrangement and orientation in the transition space, and nanoscale stress analysis that stabilizes the hcp structure. Crucially, dynamic shock loading deposits excess energy, allowing the phase transition to arrest at a metastable structure featuring coherent hcp nuclei. This behavior contrasts sharply with quasi-static deformation paradigms[28,49,50] and establishes a novel transformation pathway that bypasses classical phase-transition barriers.

## Methods

### Materials: 4N single-crystal Fe

The 4N single-crystal Fe samples (99.99 wt % purity) used in this study were commercially obtained from MaTeck GmbH, provided as discs with a diameter of 15 mm and height of 2 mm (⌀ 15×2 mm). These crystals possess a (110) surface orientation, with the normal direction (ND) aligned along the [110] crystallographic axis. Detailed information on the crystallographic orientation and properties is presented in Fig. 1b. For SHPB experiments, the single-crystal Fe samples were further reduced in size via wire cutting to final dimensions of ⌀3×2 mm.

### SHPB experiments

Consistent with our prior methodology[38], a cryogenic furnace system maintained target temperatures via precisely regulated liquid nitrogen vapor flow. The vapor rate was controlled via a heating wire system inside the liquid nitrogen bottle, allowing automated adjustment based on the power input. This system ensured reliable temperature regulation throughout the experiment. As shown in Fig. 1a, the heating mechanism maintains a stable low-temperature environment by moderating the vapor release, thereby sustaining consistent experimental conditions. The 4N single-crystal Fe samples were sectioned into cylindrical geometries via electrical discharge wire-cutting (EDWC), with final dimensions precisely matching those in Fig. 1b. All circumferential and end surfaces were mirror-finished through sequential grinding with SiC abrasive papers (400 to 5000 grit) followed by colloidal silica polishing (0.05 μm). The sample was initially cooled in liquid nitrogen for 30 minutes before being swiftly positioned between the incident and transmission bars (dimensions: ⌀14.5 × 1,000 mm) using tweezers. During the Split-Hopkinson Pressure Bar (SHPB) test, a gas-accelerated projectile (⌀14.5 × 300 mm) shocked the incident bar at 38 m/s, generating a compressive stress wave that propagated from the shock surface to the

sample. At the interface between the incident bar and the sample, part of the wave reflected back as a reflected wave, while the remaining portion continued through the sample into the transmission bar.

To capture the incident, reflected, and transmitted waves, standard strain gauges were used, and the resulting data were recorded by an oscilloscope (Tektronix MDO 3024), as illustrated in Fig. 1a. From these recorded waveforms, engineering stress-strain and strain rate-strain curves were derived (Supplementary Fig. 5). Under these test conditions, the engineering stress reached up to 17.6 GPa, with a maximum strain rate of $1.96 \times 10^4$ /s.

**EBSD experiments**

A TESCAN MIRA3 Nordlys Max3 scanning electron microscope (SEM), equipped with an EDAX Max EBSD detector, was used for EBSD scans at an operating voltage of 20 kV. Scans were performed with step sizes ranging from 0.08 to 0.3 μm. Following mounting in conductive resin, specimens were mechanically ground using SiC abrasive papers progressively from 400 to 5000 grit. Subsequent polishing was performed with diamond suspension, followed by 10-hour vibratory polishing with non-abrasive synthetic cloth. A final electrolytic etching step was applied to remove surface contaminants and deformation layers. Orientation maps, pole figures, and misorientation maps were then generated using AZtec EBSD analysis software, allowing for in-depth analysis of crystalline structures and orientation distributions.

Beyond localized microstructural analysis, EBSD was employed for large-area crystallographic characterization to resolve full-surface orientation signatures. While maintaining high spatial resolution, the region of interest was partitioned into multiple tiles scanned sequentially. Each tile overlapped adjacent areas by 5-10%, enabling precise stitching through orientation features within overlapping zones. This approach yielded comprehensive orientation

mapping across the entire surface, revealing macroscopic texture gradients and orientation correlations, as shown in Fig. 1f and g.

**FIB experiments**

A TESCAN AMBER SEM-Focused Ion Beam (FIB) system was employed to prepare specimens for Transmission Electron Microscopy (TEM) and aberration-corrected Scanning Transmission Electron Microscopy (ac-STEM). To suppress magnetic domain interference, samples were thinned to 80 nm for TEM analysis and further reduced to 60 nm to enhance ac-STEM image resolution (Supplementary Fig. 1b-e). Critically, all TEM specimens were sectioned perpendicular to the sample cross-section, ensuring the predominant orientation of the final lamellae aligned parallel to the (111) planes. For three-dimensional Atom Probe Tomography (3D-APT), FIB milling was conducted normal to the sample surface to distribute (111) planes transversely along the needle apex (Supplementary Fig. 1f-i). The resulting needle-shaped specimens featured heights ≤300 nm with tip diameters <100 nm. A redundant length was preserved at the needle base to prevent fracture during transfer, with three independent fabrication trials performed to mitigate potential failures during APT analyses.

**TEM and related analysis**

A Talos F200X G2 Transmission Electron Microscope (TEM) was utilized to analyze the sample's microstructure. This TEM achieves a high-resolution transmission electron microscopy (HRTEM) linear resolution of 0.10 nm and a Scanning Transmission Electron Microscopy (STEM) resolution of 0.14 nm. For compatibility with the instrument's specimen holder, the sample was sectioned into circular slices with a 3 mm diameter, enabling imaging of larger-scale micrographs. Initial attempts to capture High-Angle Annular Dark-Field Scanning Transmission Electron Microscopy (HAADF-STEM) images were limited by the F200X's resolution and magnetic

interference from the relatively large sample, resulting in insufficient clarity to distinctly resolve the hcp ε-Fe structure.

After additional processing using FIB techniques, the sample's size and thickness were further reduced, overcoming previous size constraints and mitigating magnetic interference. This refinement enabled clearer STEM imaging. As shown in Supplementary Fig. 4 and Supplementary Fig. 6, the STEM results of the processed sample revealed characteristic hcp (0001) ring-like features, offering valuable insights into the phase transition process.

**Ac-STEM experiments**

A JEOL NEOARM 200F ac-TEM, paired with a JEOL JED2300 Energy Dispersive Spectrometer (EDS) detector, was utilized to capture High-Angle Annular Dark-Field Scanning Transmission Electron Microscopy (HAADF-STEM) images. Operating at an accelerating voltage of 200 kV, the setup achieved a resolution of 0.078 nm with an energy divergence of 0.5 eV. These parameters enabled the clear visualization of the hcp ε-Fe atomic structure, specifically revealing detailed atomic arrangements. Atomic-scale EDS analysis was conducted to examine the high-purity Fe sample, focusing on the hcp (0001) ring-like structure, confirming the phase transition from bcc to hcp without any impurities. The EDS results verified the chemical purity and structural integrity of the Fe crystal throughout the transformation process.

In this study, we conducted multiple multi-condition verification experiments on single-crystal Fe samples. Ac-STEM characterization exceeding 100 hours revealed stable hcp structures at different locations. All observed hcp phases exhibited a strict size constraint within 30 nm, indicating that the nucleation mechanism of hcp structure imposes dimensional limitations. This size-dependent behavior was further validated through subsequent nanoscale stress concentration analysis.

## APT experiments

A CAMECA LEAP 6000XR APT system was employed to investigate the three-dimensional atomic distribution of the sample. The experiment was conducted at 50 K to minimize thermal diffusion during analysis. The APT system's maximum data collection speed, exceeding 4 million ions per minute, enabled high-resolution mapping of the atomic structure. This setup provided precise insights into the spatial distribution and composition of the material, allowing for a detailed examination of the uniformity of Fe atoms and the absence of impurities within the hcp ε-Fe structure.

**Data availability:** The data that support the findings of this study are available within this article and its Supplementary Information. Further data are available from the corresponding authors upon request.

## References


1. Branch, B. A. & Jensen, B. J. Dynamic x-ray diffraction to study the shock-induced α-ε phase transition in iron. *AIP Conference Proceedings* **1979**, (2017).
2. Tateno, S., Hirose, K., Ohishi, Y. & Tatsumi, Y. The Structure of Iron in Earth's Inner Core. *Science* **330**, 359–361 (2010).
3. Vočadlo, L. *et al.* Possible thermal and chemical stabilization of body-centred-cubic iron in the Earth's core. *Nature* **424**, 536–539 (2003).
4. Wenk, H. R., Matthies, S., Hemley, R. J., Mao, H. K. & Shu, J. The plastic deformation of iron at pressures of the Earth's inner core. *Nature* **405**, 1044–1047 (2000).
5. Deluigi, O. R. & Bringa, E. M. Mechanical properties of hcp Fe at high pressures and temperatures from large-scale molecular dynamics simulations. *Journal of Applied Physics* **136**, (2024).
6. Friák, M. & Šob, M. Ab initio study of the bcc-hcp transformation in iron. *Physical Review B* **77**, 174117 (2008).

7. Saxena, S. S. & Littlewood, P. B. Iron cast in exotic role. *Nature* **412**, 290–291 (2001).
8. Jaccard, D., Holmes, A. T., Behr, G., Inada, Y. & Onuki, Y. Superconductivity of ε-Fe: complete resistive transition. *Physics Letters A* **299**, 282–286 (2002).
9. Gavriliuk, A. G. *et al.* Electronic and Magnetic Properties of the ε-Fe Phase at High Pressures up to 241 GPa in the Temperature Range of 4–300 K. *JETP Letters* **117**, 126–137 (2023).
10. Saxena, S. K., Shen, G. & Lazor, P. Experimental Evidence for a New Iron Phase and Implications for Earth's Core. *Science* **260**, 1312–1314 (1993).
11. Kraus, R. G. *et al.* Measuring the melting curve of iron at super-Earth core conditions. *Science* **375**, 202–205 (2022).
12. Wang, K., Xiao, S., Deng, H., Zhu, W. & Hu, W. An atomic study on the shock-induced plasticity and phase transition for iron-based single crystals. *International Journal of Plasticity* **59**, 180–198 (2014).
13. Shao, J.-L., Wang, P., Zhang, F.-G. & He, A.-M. Effects of temperature and void on the dynamics and microstructure of structural transition in single crystal iron. *Journal of Physics: Condensed Matter* **30**, 255401 (2018).
14. Merkel, S., Lincot, A. & Petitgirard, S. Microstructural effects and mechanism of bcc-hcp-bcc transformations in polycrystalline iron. *Physical Review B* **102**, 104103 (2020).
15. Loree, T. R., Warnes, R. H., Zukas, E. G. & Fowler, C. M. Polymorphism of Shock Loaded Fe-Mn and Fe-Ni Alloys. *Science* **153**, 1277–1278 (1966).
16. Bancroft, D., Peterson, E. L. & Minshall, S. Polymorphism of Iron at High Pressure. *Journal of Applied Physics* **27**, 291–298 (1956).
17. Saxena, S. K. *et al.* Synchrotron X-Ray Study of Iron at High Pressure and Temperature. *Science* **269**, 1703–1704 (1995).
18. Komabayashi, T. & Fei, Y. Internally consistent thermodynamic database for iron to the Earth's core conditions. *Journal of Geophysical Research: Solid Earth* **115**, (2010).
19. Vattré, A. & Denoual, C. Polymorphism of iron at high pressure: A 3D phase-field model for displacive transitions with finite elastoplastic deformations. *Journal of the Mechanics and Physics of Solids* **92**, 1–27 (2016).
20. Shao, J.-L., Wang, P., Zhang, F.-G. & He, A.-M. Hcp/fcc nucleation in bcc iron under different anisotropic compressions at high strain rate: Molecular dynamics study. *Scientific Reports* **8**, 7650 (2018).

21. Mao, H. K., Wu, Y., Chen, L. C., Shu, J. F. & Jephcoat, A. P. Static compression of iron to 300 GPa and Fe0.8Ni0.2 alloy to 260 GPa: Implications for composition of the core. *Journal of Geophysical Research: Solid Earth* **95**, 21737–21742 (1990).

22. Luo, W. *et al.* Dynamical stability of body center cubic iron at the Earth's core conditions. *Proceedings of the National Academy of Sciences* **107**, 9962–9964 (2010).

23. Mikhaylushkin, A. S. *et al.* Pure Iron Compressed and Heated to Extreme Conditions. *Physical Review Letters* **99**, 165505 (2007).

24. Jensen, B. J., Gray, G. T. & Hixson, R. S. Direct measurements of the α-ϵ transition stress and kinetics for shocked iron. *Journal of Applied Physics* **105**, (2009).

25. Stixrude, L. Structure of Iron to 1 Gbar and 40 000 K. *Physical Review Letters* **108**, 055505 (2012).

26. Ping, Y. *et al.* Solid Iron Compressed Up to 560 GPa. *Physical Review Letters* **111**, 065501 (2013).

27. Anzellini, S., Dewaele, A., Mezouar, M., Loubeyre, P. & Morard, G. Melting of iron at Earth's inner core boundary based on fast X-ray diffraction. *Science* **340**, 464–6 (2013).

28. Wang, S. J. *et al.* Microstructural fingerprints of phase transitions in shock-loaded iron. *Scientific Reports* **3**, 1086 (2013).

29. Hawreliak, J. A. & Turneaure, S. J. Observations of twinning microstructure in iron ramp-compressed through the phase transition. *Physical Review B* **106**, 174306 (2022).

30. Hawreliak, J. A. *et al.* Analysis of the x-ray diffraction signal for the {alpha}-{epsilon} transition in shock-compressed iron: Simulation and experiment. *Physical Review B* **74**, 184107 (2006).

31. Kalantar, D. H. *et al.* Direct Observation of the α-ε Transition in Shock-Compressed Iron via Nanosecond X-Ray Diffraction. *Physical Review Letters* **95**, 075502 (2005).

32. Walsh, J. M. & Christian, R. H. Equation of state of metals from shock wave measurements. *Physical Review* **97**, 1544–1556 (1955).

33. Duff, R. E. & Minshall, F. S. Investigation of a Shock-Induced Transition in Bismuth. *Physical Review* **108**, 1207–1212 (1957).

34. Barker, L. M. & Hollenbach, R. E. Shock wave study of the α ⇄ ε phase transition in iron. *Journal of Applied Physics* **45**, 4872–4887 (1974).

35. de Rességuier, T. & Hallouin, M. Effects of the α-ε phase transition on wave propagation and spallation in laser shock-loaded iron. *Physical Review B* **77**, 174107 (2008).

36. Hawreliak, J. A. *et al.* In situ x-ray diffraction measurements of the c/a ratio in the high-pressure ε phase of shock-compressed polycrystalline iron. *Physical Review B* **83**, 144114 (2011).
37. Yaakobi, B. *et al.* EXAFS Measurement of Iron bcc-to-hcp Phase Transformation in Nanosecond-Laser Shocks. *Physical Review Letters* **95**, 075501 (2005).
38. Liu, M. *et al.* Deformation-activated recrystallization twin: New twinning path in pure aluminum enabled by cryogenic and rapid compression. *iScience* **25**, 104248 (2022).
39. Nairong TAO, K. L. Dynamic Plastic Deformation (DPD): A Novel Technique for Synthesizing Bulk Nanostructured Metals. *J. Mater. Sci. Technol.* **23**, 771–774 (2007).
40. Chen, M. *et al.* Deformation Twinning in Nanocrystalline Aluminum. *Science* **300**, 1275–1277 (2003).
41. Zhang, J. *et al.* Timely and atomic-resolved high-temperature mechanical investigation of ductile fracture and atomistic mechanisms of tungsten. *Nature Communications* **12**, 2218 (2021).
42. Pan, Q. *et al.* Atomic faulting induced exceptional cryogenic strain hardening in gradient cell–structured alloy. *Science* **382**, 185–190 (2023).
43. Li, C., Liu, Z., Goonetilleke, E. C. & Huang, X. Temperature-dependent kinetic pathways of heterogeneous ice nucleation competing between classical and non-classical nucleation. *Nature Communications* **12**, 4954 (2021).
44. McGraw, R. L., Winkler, P. M. & Wagner, P. E. Temperature Dependence in Heterogeneous Nucleation with Application to the Direct Determination of Cluster Energy on Nearly Molecular Scale. *Scientific Reports* **7**, 16896 (2017).
45. Hwang, H. *et al.* Subnanosecond phase transition dynamics in laser-shocked iron. *Science Advances* **6**, eaaz5132 (2020).
46. Pang, W. W., Zhang, P., Zhang, G. C., Xu, A. G. & Zhao, X. G. Nucleation and growth mechanisms of hcp domains in compressed iron. *Sci Rep* **4**, 5273 (2014).
47. Hu, J. *et al.* Experimental and atomic observations of phase transformations in shock-compressed single-crystal Fe. *Materialia* **20**, 101200 (2021).
48. Hawreliak, J. A. & Turneaure, S. J. Probing the lattice structure of dynamically compressed and released single crystal iron through the alpha to epsilon phase transition. *Journal of Applied Physics* **129**, (2021).
49. Kadau, K., Germann, T. C., Lomdahl, P. S. & Holian, B. L. Atomistic simulations of shock-induced transformations and their orientation dependence in bcc Fe single crystals. *Physical Review B* **72**, 064120 (2005).

50. Amadou, N., de Resseguier, T., Dragon, A. & Brambrink, E. Coupling between plasticity and phase transition in shock- and ramp-compressed single-crystal iron. *Physical Review B* **98**, 024104 (2018).

535

## Acknowledgments

This work is supported by the National Natural Science Foundation of China (Grant No. 11872361) and the Start-up Grant from Northeastern University in China (Grant No. 01270021920501*106).

The authors thank all the engineers who have assisted with the observations reported in this paper, especially Y. K. and W. X. in Liaoning Academy of Materials for the APT experiments and processing the data.

## Author information

These authors contributed equally: Jiamu Liu, Jianxing Liu, Pengfei Wang

**Author Contributions:**

M. L. conceptualized the project, supervised the research, and contributed to methodology development, funding acquisition, project administration, and writing (both original draft preparation and review & editing). J. M. L. led methodology design, conducted investigation, visualized results, co-managed the project, and participated in writing (original draft and review & editing). J. W. contributed to methodology, investigation, supervision, and writing (review & editing). H. D., P. F. W., J. X. L., T. T. H., and M. Y. G. performed the investigation; among them, P. F. W. assisted in drafting the original manuscript, and J. X. L. secured funding support. All authors have given final approval for the published version.

**Corresponding authors:**

Correspondence to Jian Wang and Mao Liu

## Ethics declarations

**Competing interest declaration:** Authors declare that they have no competing interests.

# Additional information

### Supplementary information

Supplementary Text and Supplementary Figs. 1–6.

# Supplementary Text

### APT analysis

In this study, beyond observing elemental Fe distribution in APT maps—confirming phase transformation stems purely from structural rearrangement—we performed pole reconstruction on deformed single-crystal Fe specimens. Using bcc (111) planes identified via STEM as reference axes, orientation imaging microscopy (OIM) analysis perpendicular to the STEM sampling direction revealed a 3D architecture of parallel (111) planes distributed radially along the needle apex. This spatial configuration aligns with prior EBSD and STEM results.

Pole reconstruction enables crystallographic characterization from reconstructed atomic data. Although complete crystal information may not be directly attainable, key features can be inferred: atomic planes emerge in reconstructed datasets, and statistical techniques account for minor deviations of atoms from ideal lattice sites. Despite inherent APT has limitations that the spatial offsets during field evaporation may distort absolute positions. Data correction compensates for distortions introduced during acquisition and analysis[51,52].

The principle is that sample's overall crystal structure is typically preserved by Fourier

Transform (FT) based periodicity detection[53]. FT identifies global periodic structures by converting real-space atomic positions into reciprocal space, where lattice plane signals intensify[54].

The equation that defines the FT of a three-dimensional real-space function $\boldsymbol{r}(x, y, z)$ into reciprocal space $\boldsymbol{R}(X, Y, Z)$ is:

$$F(R) = \iiint f(r) e^{-2\pi i(r \cdot R)} \, dxdydz \tag{1}$$

Applying the Dirac delta function yields the atomic grid position formula:

$$f(r) = \sum_{i=1}^{N} \delta(r - r_i) \tag{2}$$

Written as

$$F(R) = \sum_{i=1}^{N} e^{-2\pi i(r_i \cdot R)} \tag{3}$$

Spatial distribution maps (SDM) characterize interplanar spacing $d^{\{hkl\}}$ along the depth direction and angles $\theta^{\{hkl\}}$ and $\varphi^{\{hkl\}}$ between crystal planes and coordinate axes. Transverse SDM analysis resolves local atomic neighborhoods, retaining crystallographic data. Here, z-SDM reconstruction of Fe atoms confirmed (111) plane distribution.

AP Suite software is used for the visualization:

(1) OIM-guided orientation locking: Manually defining the crystallographic orientation (111) to establish a reference frame, requiring expertise to ensure accuracy.

(2) Orientation-based filtering: Selecting atoms with proper the target on (111) plane.

(3) 3D reconstruction and rotation: Aligning the atomic cloud perpendicular to (111) planes to verify the correct interplanar spacing.

Critically, heterogeneous zones in the 3D pole reconstruction (Fig. 3b) cannot be definitively attributed to hcp Fe. Since reconstruction relies on (111) plane alignment, and hcp-bcc interfaces are coherent, position-correction algorithms may inadvertently realign hcp atoms. Thus, atomic

clusters deviating from (111) aggregation patterns were not classified as hcp domains, pending correlated TEM validation.

**EBSD analysis**

EBSD mapping for 77 K (Fig. 1f and Supplementary Fig. 2b) and room temperature (Fig. 1g and Supplementary Fig. 2a) reveals a reorientation from predominant (110) to (111) textures. The microstructure exhibits a divergent crystallographic colonies distribution: fine grains with randomized orientations dominate the central region, while radially distributed (001) oriented streaks propagate from the core toward the periphery, terminating within the (111) textured matrix. High-magnification analysis (Supplementary Fig. 2) demonstrates that the 77K sample contains over an order of magnitude more fine grains than the room-temperature counterpart, with average grain size reduced by approximately 50%.

**Temperature dependence of phase transition in TEM**

To assess temperature dependence of hcp phase formation in bcc Fe, SHPB shock tests were conducted at room temperature (298 K) under identical projectile velocity (35.4 m/s). As revealed by TEM and HAADF-STEM imaging (Supplementary Fig. 6a and b), the crystallographic relationship—bcc (111) || hcp (0001)—remains consistent with the 77 K groups. Crucially, the cryogenic and room-temperature samples exhibit distinct hcp phase distribution characteristics. As highlighted in Supplementary Fig. 4, the 77K sample demonstrates densely clustered hcp domains. Conversely, room-temperature shocked specimens (Supplementary Fig. 6) display dispersed hcp features. This contrast underscores temperature-dependent nucleation kinetics—suppressed thermal activation at 77 K promotes localized hcp phase coalescence.

**Phase diagram and spatial orientation**

Figure 5a and b demonstrates the crystallographic correspondence between bcc and hcp

phases and three-dimensional spatial structure model determined based on this correspondence. Using established OR—bcc(111) || hcp(0001) and bcc(110) || hcp($10\bar{1}0$)—we aligned both phases' stereographic projections to their matching orientations (Fig. 5a). Within these superimposed projections, spatially coincident pole pairs were identified to determine mutually coherent interface planes between the phases.

Three low-index coherent planes (highlighted by green dashed circles in Fig. 5a) exhibit 120° rotational symmetry in the stereographic projection. These symmetry axes indicate that such coherent planes can form space-filling polyhedral configurations at phase boundaries. While these low-index planes define a fundamental crystallographic existence, realistic interfaces may incorporate additional high-index planes.

Based solely on the three symmetric planes and the primary OR bcc(111) || hcp(0001), a polyhedral structural unit was constructed (Fig. 5b). This unit which termed the transition layer, features an hcp core enclosed by coherent normal facets aligned to the identified pole pairs. Remarkably, this configuration agrees with our atomic-resolution ac-STEM observations, confirming that hcp phases exist as coherent nuclei within the transition layer, embedded epitaxially within the bcc matrix. The schematic representation depicts atomic arrangement patterns within the structure, independent of the ensemble's spatial shape or size.

**Nanoscale Stress Concentration analysis**

Geometric phase analysis (GPA) of STEM images quantified stress concentration around transition layers. Fig. 5c shows an atomic-resolution STEM micrograph containing an hcp domain (red oval), with the inset SAED pattern confirming unstrained bcc matrix diffraction conditions. As indicated by the red and blue circles with identical radii and tangentially connected, this region denotes the matrix area with an unstrained lattice. By generating local SAED patterns across the region and comparing spot displacement vectors relative to the central reference, inverse FT

yielded complex images whose phase components encoded local atomic displacements. These were converted to strain tensors using the stress-field equation[55,56]:

$$\left.\begin{aligned} u_x &= a_x e_{xx} + a_y e_{xy} \\ u_y &= a_y e_{yy} + a_x e_{yx} \end{aligned}\right\} \begin{bmatrix} e_{yx} \\ e_{yy} \end{bmatrix} = \begin{bmatrix} a_x & a_y \\ b_x & b_y \end{bmatrix}^{-1} \begin{bmatrix} u_y \\ v_y \end{bmatrix}$$
$$\left.\begin{aligned} v_x &= b_x e_{xx} + b_y e_{xy} \\ v_y &= b_y e_{yy} + b_x e_{yx} \end{aligned}\right\} \begin{bmatrix} e_{xx} \\ e_{xy} \end{bmatrix} = \begin{bmatrix} a_x & a_y \\ b_x & b_y \end{bmatrix}^{-1} \begin{bmatrix} u_x \\ v_x \end{bmatrix} \quad \text{(S4)}$$

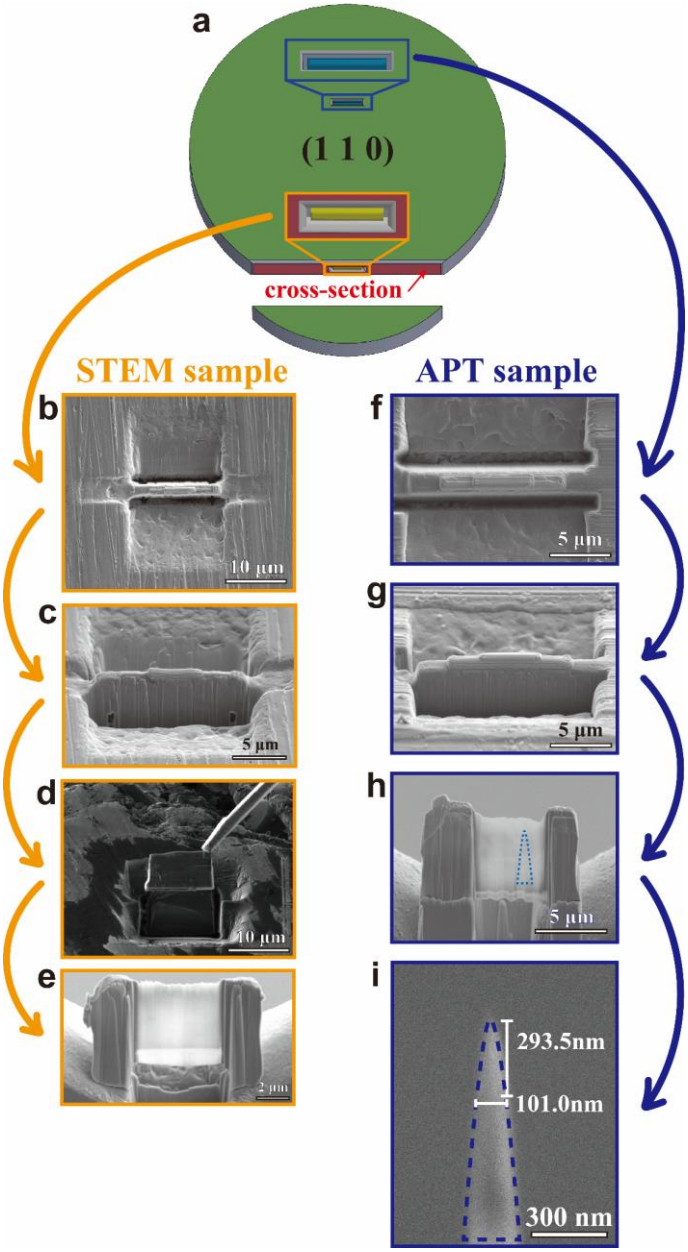
Where $(u_x, u_y)$ and $(v_x, v_y)$ are the coordinates of the displacement with respect to reference vector $\vec{a}(a_x, a_y)$ and $\vec{b}(b_x, b_y)$, respectively, and $e_{xx}$, $e_{xy}$, $e_{yy}$, and $e_{yx}$ are defined as follows:

$$e_{xx} = \frac{\partial_u}{\partial_x}, e_{xy} = \frac{\partial_u}{\partial_y}, e_{yy} = \frac{\partial_v}{\partial_y}, e_{yx} = \frac{\partial_v}{\partial_x} \quad \text{(S5)}$$

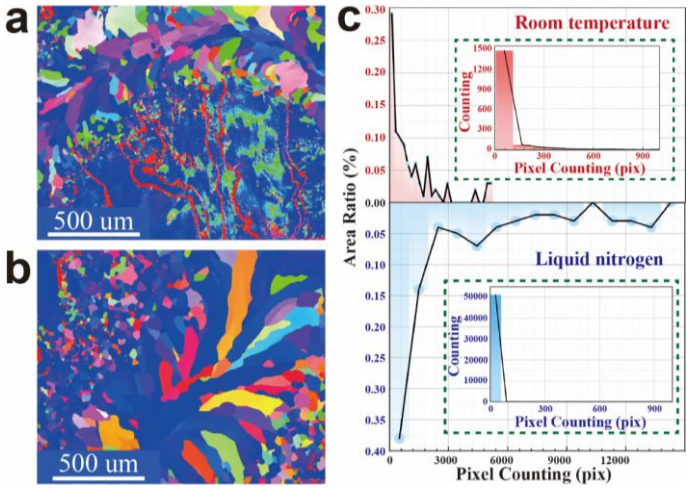
Figure 5d displays the $e_{xy}$ strain component, revealing intense stress confinement surrounding the hcp nucleus, showing a signature of thermodynamic stability. Atomic-scale tracking of the bcc to hcp transition pathway (Fig. 5e-h) identified two distinct atomic slip directions within the (111) plane: perpendicular and parallel to the phase transition direction. These displacements represent projections of shear-induced transformation mechanisms, consistent with shock-mediated kinetics.

Critically, the observed microstructures are not static transition snapshots but dynamically arrested states. Unlike quasi-static transformations, ultrahigh-strain-rate shock loading causes instantaneous phase progression, and the core exhibits complete hcp conversion, while peripheral regions retain increasing bcc character with distance from the nucleus.

## Supplementary Figure

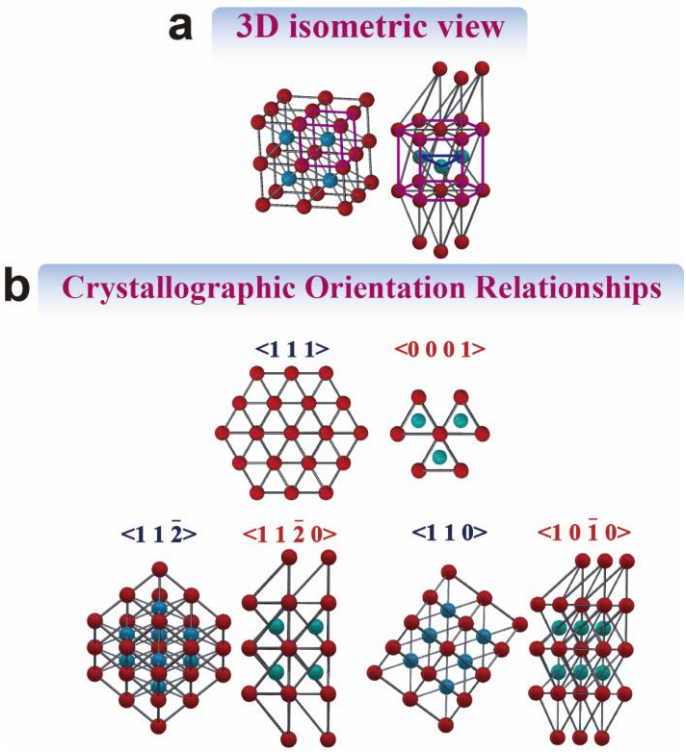



**Supplementary Fig. 1 FIB preparation of samples for correlative STEM and APT analysis.** (**a**) Schematic of STEM and APT sampling locations. The orange frame highlights the STEM sampling site normal to sample cross-section. The blue frame highlights APT sampling site normal to (110) crystallographic plane. (**b-e**) Sample was processed by FIB, welded onto a copper TEM grid via Pt deposition, and prepared for TEM/STEM characterization. (**f-i**) APT sample was processed by FIB, and the final needle tip exhibits a smooth morphology with approximately 300 nm in height and 100 nm in diameter.

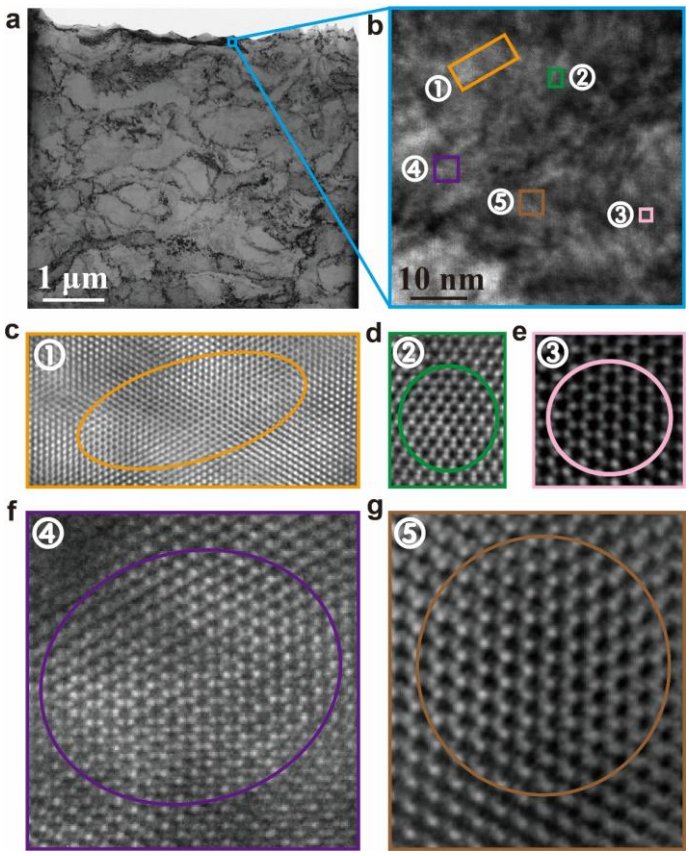



675

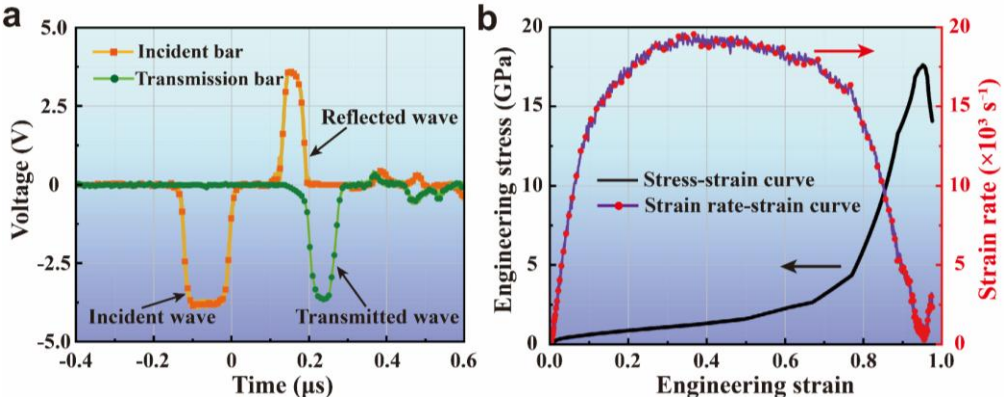
**Supplementary Fig. 2 Magnified EBSD images of the areas within the white boxes in Fig. 1g and f, showcasing the statistical analysis of grain size.** (**a**) EBSD at room temperature. (**b**) EBSD at 77K. (**c**) Grain pixel counting of samples at room temperature and liquid nitrogen.



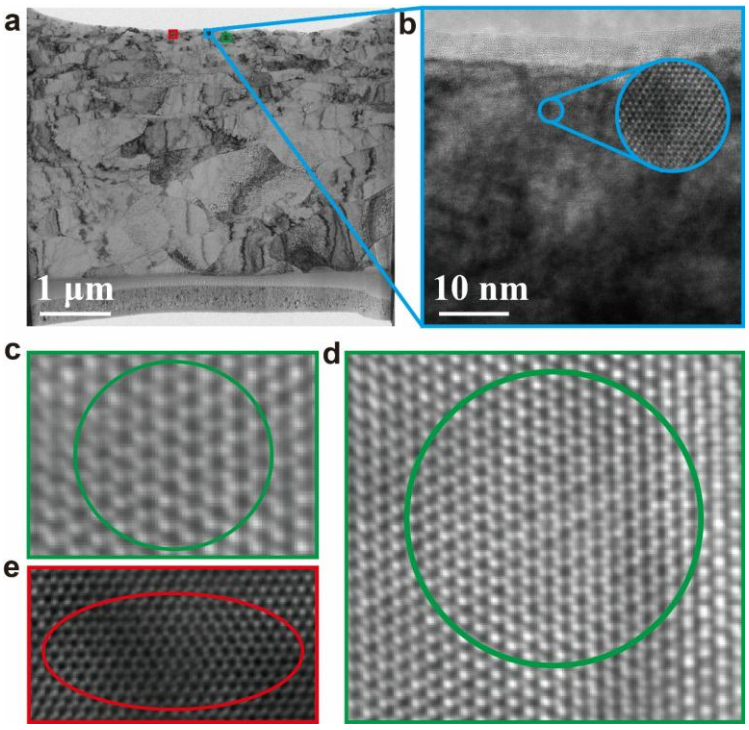

**Supplementary Fig. 3 Structural diagram of crystallographic orientation relationship.** (**a**) 3D isometric view of bcc Fe and hcp Fe. (**b**) Crystallographic orientation relationships of bcc (111) || hcp (0001), bcc $(11\bar{2})$ || hcp $(11\bar{2}0)$ and bcc (110) || hcp $(10\bar{1}0)$.




**Supplementary Fig. 4 HAADF-STEM images showing the phase transition of bcc (111) || hcp (0001) at 77K.** (**a**) TEM image of the FIB-milled sample at large-scale, the blue box denotes the magnified area. (**b**) Magnified HAADF-STEM image, and the color-coded rectangles denote regions with distinct hcp atomic arrangements, spaced approximately 10 nm apart. (**c-g**) Characteristic hcp (0001) ring-like features are highlighted with colored ovals or circles, corresponding to the positions highlighted in (**b**).




**Supplementary Fig. 5 Split-Hopkinson pressure bar (SHPB) shock compression.** (**a**) Three stress waves in SHPB test under 38m/s ($\dot{\varepsilon} = 1.96 \times 10^4\ s^{-1}$) shock loading. (**b**) Engineering stress-strain curve and strain rate-strain curve.




**Supplementary Fig. 6 HAADF-STEM images showing the phase transition of bcc (111) || hcp (0001) at room temperature.** (**a**) TEM image of the FIB-milled sample at large-scale, the colored boxes denote the magnified area. (**b**) HAADF image which is framed by blue rectangles, and the blue circle highlights an amplification of the hcp feature. (**c-e**) Characteristic hcp (0001) ring-like features, highlighted by green circles and red oval, are observed in the areas corresponding to green and red rectangles highlighted in (**a**). These features exhibit a more discrete distribution of hcp characteristics compared to the liquid nitrogen group.

## Supplementary References


51. Gault, B. *et al.* Advances in the calibration of atom probe tomographic reconstruction. *Journal of Applied Physics* **105**, (2009).
52. Gault, B., Moody, M. P., Cairney, J. M. & Ringer, S. P. *Atom Probe Microscopy*. vol. 160 (Springer New York, New York, NY, 2012).
53. W. A. Sethares & T. W. Staley. Periodicity transforms. *IEEE Transactions on Signal Processing* **47**, 2953–2964 (1999).
54. Warren, P. J., Cerezo, A. & Smith, G. D. W. An atom probe study of the distribution of rhenium in a nickel-based superalloy. *Materials Science and Engineering: A* **250**, 88–92 (1998).
55. Galindo, P. L. *et al.* The Peak Pairs algorithm for strain mapping from HRTEM images. *Ultramicroscopy* **107**, 1186–1193 (2007).
56. Hÿtch, M. J., Snoeck, E. & Kilaas, R. Quantitative measurement of displacement and strain fields from HREM micrographs. *Ultramicroscopy* **74**, 131–146 (1998).

# Supplementary Files

This is a list of supplementary files associated with this preprint. Click to download.

- supplementaryinformation.docx